

Comparison between lidar and nephelometer
measurements of aerosol hygroscopicity at the
Southern Great Plains Atmospheric Radiation
Measurement site

August 9, 2004

M. Pahlow, G. Feingold

NOAA, Environmental Technology Laboratory, Boulder, Colorado, USA

A. Jefferson, E. Andrews, J.A. Ogren

NOAA, Climate Monitoring and Diagnostics Laboratory, Boulder,
Colorado, USA

J. Wang, Y.-N. Lee

Brookhaven National Laboratory, Upton, New York, USA

R. A. Ferrare

NASA, Langley Research Center, Hampton, Virginia, USA

To be submitted to *J. Geophys. Res.*

Corresponding Author Address:

Markus Pahlow

NOAA/ETL/ET2

325 Broadway, Boulder, CO 80305, USA

Phone: +1 (303) 497-4437

Fax: +1 (303) 497-5318

Email: markus.pahlow@noaa.gov

Abstract

Aerosol hygroscopicity has a significant effect on radiative properties of aerosols. Here a lidar method, applicable to cloud-capped, well-mixed atmospheric boundary layers, is employed to determine the hygroscopic growth factor $f(\text{RH})$ under unperturbed, ambient atmospheric conditions. The data used for the analysis were collected under a wide range of atmospheric aerosol levels during both routine measurement periods and during the intensive operations period (IOP) in May 2003 at the Southern Great Plains (SGP) field site in Oklahoma, USA, as part of the Atmospheric Radiation Measurement (ARM) program. There is a good correlation (~ 0.7) between a lidar-derived growth factor (measured over the range 85% RH to 96% RH) with a nephelometer-derived growth factor measured over the RH range 40% to 85%. For these RH ranges, the slope of the lidar-derived growth factor is much steeper than that of the nephelometer-derived growth factor, reflecting the rapid increase in particle size with increasing RH. The results are corroborated by aerosol model calculations of lidar and nephelometer equivalent $f(\text{RH})$ based on *in situ* aerosol size and composition measurements during the IOP. It is suggested that the lidar method can provide useful measurements of the dependence of

aerosol optical properties on relative humidity, and under conditions closer to saturation than can currently be achieved with humidified nephelometers.

1 Introduction

The importance of atmospheric aerosols for the Earth’s climate has been widely recognized (e.g. Charlson et al., 1992; Boucher and Anderson, 1995; Vogelmann et al., 2003). They affect solar radiation and hence climate through the “direct effect” by scattering radiation back to space (Charlson et al., 1992), but also through the “indirect effect” where they can act as cloud condensation nuclei (Twomey, 1974). An important factor affecting the role aerosols play in climate change is their hygroscopicity. The swelling of aerosols due to water vapor uptake will enhance their ability to scatter radiation. Numerous studies have investigated the relationship between aerosol scattering and relative humidity in terms of the hygroscopic growth factor $f(\text{RH})$ using humidified nephelometers. These have been used for airborne or ground-based determination of the growth factor over a range of relative humidity RH from 20%–40% and up to 90% (e.g. McInnes et al., 1998; Kotchenruther et al., 1999; Malm et al., 2003). Humidified Tandem Differential Mobility Analyzers (HTDMAs) allow one to determine aerosol hygroscopicity as a function of particle size, usually for RH up to $\sim 90\%$ (e.g. McMurry and Stolzenburg, 1989; Covert and Heintzenberg, 1993; Brechtel and Kreidenweis, 2000). The lidar (light detection and ranging) technique

provides the opportunity to investigate hygroscopic growth of aerosols beyond this RH range, under ambient atmospheric conditions and without perturbing the sampled air. Ferrare et al. (1998) used Raman lidar to simultaneously measure aerosol backscatter and RH in a study that demonstrated the capability of lidar to measure $f(\text{RH})$. Wulfmeyer and Feingold (2000) used differential absorption lidar to measure the enhancement in backscatter in the regime of high RH up to $\sim 98.5\%$. More recently Feingold and Morley (2003) (henceforth FM) used elastic backscatter lidar data combined with thermodynamic assumptions of the mixing state of the atmosphere to determine $f(\text{RH})$ for RH up to $\sim 98.5\%$. In this paper we make use of this combined lidar-thermodynamic approach to determine $f(\text{RH})$ for relative humidities close to saturation and for a broad range of atmospheric aerosol conditions. We apply this method for a much broader range of aerosol conditions than has been done in the past. The analysis by Wulfmeyer and Feingold (2000) was limited to a one-minute time period and FM analyzed 30 minutes worth of data. We also provide first comparisons with a ground-based nephelometer-derived $f(\text{RH})$ and show that there is a strong correlation between these two independently derived growth factors. In addition, we show that there is broad consistency between lidar and nephelometer growth factors and those

computed from *in situ* aerosol size distribution and from in-situ aerosol size distribution and composition measurements during the IOP.

2 Experiment

The data used for our analysis were collected between 1998–2003 both during routine measurement periods and during the intensive operations period (IOP) in May 2003, at the Southern Great Plains (SGP) field site in Oklahoma, USA (latitude +36.605, longitude -97.489 ; elevation: 315 m asl), as part of the Atmospheric Radiation Measurement (ARM) program. We utilize CART (Cloud and Radiation Testbed) Raman lidar data (355 nm), three wavelength (450 nm, 550 nm and 700 nm) nephelometer data (two TSI models 3563, one of them humidified - called a humidograph, sampling aerosol particles with a diameter of $\leq 10 \mu\text{m}$), light absorption photometer data at 565 nm (Radiance Research model PSAP), as well as micrometeorological data. During the IOP we also use data from a differential mobility analyzer (DMA; TSI model 3081), tapered-element oscillating microbalance (TEOM; Rupprecht and Patashnick Series 1400a) and a particle-into-liquid sampler (PILS; Orsini et al., 2003). The CART Raman lidar is a self-contained, fully

computer-automated system designed for unattended, continuous profiling of water vapor, aerosols and clouds at the SGP site (Goldsmith et al., 1998). The light source is a frequency-tripled Nd:YAG laser, operating at 30 Hz with 400 millijoule pulses to transmit light at 355 nm. The vertical range resolution is 39 m and the time resolution is 10 minutes, after averaging. The light scattering (nephelometer) and absorption (light absorption photometer) measurements used here are one-hour averages. The humidograph data are collected over a \sim 1-hour period, during which the RH is ramped up between \sim 30% and \sim 85%. The DMA samples at 2 minute intervals over a particle size range from 27.61 nm to 815.26 nm. TEOM and PILS are measured over 8 minute intervals and interpolated to 5 minute intervals. Supporting micrometeorological data (potential temperature θ and specific humidity q) are collected at one-minute intervals and at a height of 60 m above ground level.

3 Method

To determine a growth factor $f(\text{RH})_\beta$ from Raman lidar backscatter profiles and micrometeorological *in situ* data we employ thermodynamic assump-

tions for a cloud-capped, well-mixed boundary layer suggested by FM. For the approach to be applicable, the boundary layer must be well-mixed in potential temperature θ , specific humidity q , and aerosol. The latter guarantees that enhancement in backscatter with increasing vertical range is due to water vapor uptake, rather than to the existence of layers of aerosol or poorly defined RH. It is assumed that cloud base z_{cb} corresponds to 100% RH. Using an iterative procedure the vertical profile of RH can be computed starting from the *in situ* measurement of θ and q at $z = 60$ m in the following way. Successive height levels z_i are computed according to the hypsometric equation (Dutton, 1976, p. 64)

$$z_{i+1} = z_i + R_d \frac{T_v(z_i)}{g} \ln \left[\frac{p(z_i) + dp}{p(z_i)} \right] \quad (1)$$

where R_d is the gas constant of dry air, $T_v(z)$ is the virtual temperature (computed from θ and q which are assumed to be constant with height), g is acceleration due to gravity, $p(z)$ is atmospheric pressure and dp is a sufficiently small pressure increment to capture cloud base with high accuracy. For each z the RH is determined by

$$\text{RH}(z) = \frac{q(z)}{q_s(T)} \quad (2)$$

where the saturation water vapor mixing ratio is defined as

$$q_s(T) = \frac{0.622e_s(T)}{p(z) - e_s(T)} \quad (3)$$

and the saturation vapor pressure $e_s(T)$ is computed according to Magnus' formula (Iribarne and Godson, 1973, p. 63). The iterative procedure is carried out until $q = q_s(T)$, i.e. until cloud base is reached. Note that we do not make use of a lidar measure of cloud base as the relatively coarse range resolution of 39 m of the CART Raman lidar would introduce additional error in the determination of $f(\text{RH})_\beta$.

Combining the $\text{RH}(z)$ profiles from the thermodynamic approach with profiles of the backscatter coefficient $\beta(z)$ from the Raman lidar enables one to calculate

$$f(\text{RH})_\beta = \beta(\text{RH})/\beta(\text{RH}_{ref}) \quad (4)$$

which expresses the aerosol growth factor in terms of lidar backscatter at a given RH, relative to that at some lower RH_{ref} . Two and three parameter fits $\beta(\text{RH})/\beta(\text{RH}_{ref}) = a[1 - (\text{RH}/100)]^{-b}$ (Kasten, 1969) and $\beta(\text{RH})/\beta(\text{RH}_{ref}) = a[1 + b(\text{RH}/100)^c]$ (Kotchenruther and Hobbs, 1998), respectively, are applied to the data. We select either the two or three parameter fit according to which provides the best χ^2 goodness of fit. The fit allows us to determine $f(\text{RH})_\beta$ for specific RH values. Similarly these fit equations are also used

to determine nephelometer $f(\text{RH})_{\text{neph}}$. To apply the method, the data set was first searched for cloud-capped, well-mixed cases. In order to determine whether the boundary layer was well-mixed we inspected θ and q profiles from radiosoundings, as well as the β profiles from lidar data. Furthermore, for the cases selected, it was ascertained that the θ and q measurements at $z = 60$ m were obtained above the surface layer and in the mixed layer. An additional data selection criterion was the accuracy of the cloud base determination using the thermodynamic assumptions. Simulations with a one-dimensional parcel model (see FM) show that a conservative estimate of cloud base lies in the first one-third of the region between the two points in the $\beta(z)$ profile that exhibit the strongest gradient. This definition of cloud base was used in our study. Time periods that met all the requirements were used for further analysis.

4 Results

4.1 Lidar and nephelometer $f(\text{RH})$

A total number of 17 lidar time series (3 of which were measured during the IOP) ranging from ten minutes to one hour met the selection criteria and

qualified for the comparison with nephelometer data. It should be noted that the data analyzed here were drawn from a subset of the entire 1998-2003 data set, used for a separate indirect effect study and does not reflect the total number of cases during this time period. Figure 1 illustrates that nephelometer and lidar data are complementary for typical RH measurement ranges. Nephelometry measures $f(\text{RH})$ for RH up to 85% and lidar extends the measurement range to RH close to saturation, i.e., beyond that which can currently be achieved with nephelometry. To compare lidar and nephelometer-derived $f(\text{RH})$ we first determined $f(\text{RH})_\beta$ profiles for all 17 cases from the lidar backscatter data and the RH profiles, obtained using the thermodynamic assumptions (Figure 2). The backscatter data are normalized to $\beta(85\% \text{ RH})$ and the profiles are computed up to RH=98%. Note the large range of $f(\text{RH})_\beta$ values at 98% RH ($\sim 1.5 - 4.2$), for the 17 cases under consideration. Backscatter data obtained at RH>98% are not considered here because at RH close to saturation even a small error in the determination of cloud base translates to a large error in RH and hence in $f(\text{RH})_\beta$. For example, an error of ± 10 m in z_{cb} , results in an error in $f(\text{RH})_\beta$ of $\pm \sim 12\%$ at RH=96.5% and $\pm \sim 50\%$ at 98.9% RH (FM).

For comparison with nephelometer-derived $f(\text{RH})_{neph}$ for 85%/40% RH

and at a wavelength of 450 nm we use the parameters for the fit to the lidar data (at 355 nm) up to 90%, 96% and 98% RH. We account for the different RH measurement ranges of the lidar and the nephelometer by normalizing the growth factors by their respective ranges, ΔRH (The difference in wavelengths is discussed in section 5.). Figure 3 shows the comparison between $f(\text{RH})_{neph} (85\%/40\%)/\Delta\text{RH}_{neph}$ (hereafter termed $f(\text{RH})'_{neph}$) and $f(\text{RH})_{\beta} (90\%/85\%)/\Delta\text{RH}_{\beta}$ and indicates no correlation (correlation coefficient $R=0.02$) between normalized lidar and nephelometer derived $f(\text{RH})$ for these RH ranges (humidograph data were available for 11 out of the 17 cases). For an upper limit in RH of 96%, $f(\text{RH})_{\beta} (96\%/85\%)/\Delta\text{RH}_{\beta}$ correlates well with $f(\text{RH})'_{neph}$ ($R=0.73$), shown in Figure 4. We note that the values of $f(\text{RH})_{\beta} (90\%/85\%)/\Delta\text{RH}_{\beta}$ are significantly larger than those of $f(\text{RH})'_{neph}$, reflecting the non-linear increase in growth with increasing RH as illustrated in Figure 1.

In Figure 5 $f(\text{RH})'_{neph}$ is compared to $f(\text{RH})_{\beta} (98\%/85\%)/\Delta\text{RH}_{\beta}$, with a correlation coefficient $R=0.68$. This case illustrates the fact that the lidar data contains hygroscopic growth information at increasingly larger RH, and over RH ranges that correspond to significant growth. We stress again that the confidence in the derived $f(\text{RH})_{\beta}$ decreases as RH approaches saturation

but this does not change the qualitative picture that emerges from Figs. 3–5.

4.2 Calculations based on in-situ aerosol data

To examine the relationship between lidar- and nephelometer-derived $f(\text{RH})$ we analyze aerosol size and composition measurements from the DMA, TEOM and PILS for the three days during the IOP that were deemed appropriate for this exercise. Figure 6 shows the mean aerosol size distributions for May 8, 13 and 17 measured by the DMA during the time periods that corresponds to the lidar and nephelometer measurements of $f(\text{RH})$. We interpolated the measured size distribution onto a finer grid to make it more suitable for model calculations as the Mie calculations behave non-monotonically with RH if the computational grid is too coarse. The aerosol composition for May 8, 13 and 17 in terms of mean total mass (TEOM), mean inorganic mass (PILS), and the difference between the two is shown in Figure 7 together with the mean inorganic fraction ϵ . We use the aerosol size distribution in an aerosol model (FM) to compute backscatter β and total scattering σ_{sp} as a function of RH, thus allowing us to determine lidar and nephelometer equivalent $f(\text{RH})$. The aerosol model assumes a sulfate, soot and dust mixture with proportions constrained by the measured inorganic fraction ϵ

and the measured single scattering albedo ω_o . Without knowledge of the non-inorganic aerosol, we make a rough approximation that it is insoluble, i.e., that ϵ represents the soluble mass fraction. We then perform calculations with a range of ϵ values to account for the likelihood that some of the non-inorganic fraction is soluble.

The normalized growth factors as computed from the *in situ* size distribution and composition data for May 8, 13 and 17 are plotted as colored symbols together with the measured growth factors in Figure 4. For this comparison we focus on the relationship between $f(\text{RH})_\beta (96\%/85\%)/\Delta\text{RH}_\beta$ (hereafter termed $f(\text{RH})'_\beta$) and $f(\text{RH})'_{neph}$, as we have more confidence in the data from this RH range, and because the correlation between the lidar and nephelometer is the greatest. On May 8 the normalized measured lidar and nephelometer $f(\text{RH})$ compare well with the normalized $f(\text{RH})$ computed from the *in situ* data. As noted above, the fraction of soluble material is uncertain and so the mean values are perturbed to the minimum and maximum values observed during the time period. These variations in ϵ have the effect of increasing (decreasing) both the lidar and nephelometer equivalent $f(\text{RH})$ values for increasing (decreasing) ϵ (Figure 4) but their positions do not deviate very much from the general trend because changes in ϵ affect particle scattering

and backscatter to similar degrees.

In Figure 8 both the normalized measured backscatter and normalized total scattering from lidar and nephelometer and the aerosol model calculations are shown. Note that the measured humidified nephelometer total scattering coefficient is normalized by the dry total scattering coefficient. The backscatter coefficient from the lidar has been normalized by the backscatter coefficient measured at 85% RH to make the measurements comparable. The backscatter and total scattering coefficients computed with the aerosol model were normalized by their values at 85% and 40%, respectively. Due to this different normalization procedure we stress that only the slopes, and not absolute values, are to be compared. Both measured and computed β_{norm} and σ_{norm} profiles show similar slopes for May 8, hence the good agreement in $f(\text{RH})'_{\beta}$ and $f(\text{RH})'_{neph}$ (see Figure 4). For the May 13 measurement the normalized $f(\text{RH})$ computed from *in situ* data compares well with the measured nephelometer $f(\text{RH})'_{neph}$, but it differs from the measured lidar $f(\text{RH})'_{\beta}$. Figure 8 clearly shows the steeper slope in the measured profile of β_{norm} when compared to β_{norm} computed from *in situ* data. The profile slopes for σ_{norm} are comparable for the measured and computed case. We suspect that the arrival of a frontal passage might have caused the discrep-

ancy between values measured and computed from *in situ* data. Figures 9(a) and 9(b) show the measured time series of the total scattering coefficient σ_{sp} and the time series of the absorption coefficient σ_{ap} , respectively. These time series indicate a rapid change in aerosol size and composition starting at ~ 1320 UT until ~ 1720 UT, which encompasses the lidar and nephelometer measurement period from 1620–1650 UT. Due to this rapid change in aerosol properties the surface layer and the mixed layer aerosol might have differed substantially, which could partially explain the difference in $f(\text{RH})'_\beta$ and $f(\text{RH})'_{neph}$. For May 17 the measured lidar $f(\text{RH})'_\beta$ and the computed $f(\text{RH})'_{neph}$ compare well (Figures 4 and 8). However, the slopes for the measured and computed normalized nephelometer scattering coefficients differ (Figure 8). This is reflected in a disagreement of the respective $f(\text{RH})'_\beta$ and $f(\text{RH})'_{neph}$ values (Figure 4). We note that the single scattering albedo that was used in the aerosol model was measured at a site located ~ 40 kilometers away from the SGP field site, as no absorption data were available on May 17 due to instrument downtime.

4.3 $f(\text{RH})$, \mathring{a} and ω_o

As this data set covers a broad range of atmospheric aerosol conditions it is instructive to investigate the relationship between $f(\text{RH})$ and the Ångström exponent \mathring{a} , a parameter closely related to the size distribution of the aerosol population. In 14 of the 17 cases studied here nephelometer data at 450 nm and 700 nm were available to compute \mathring{a} . In Figure 10, $f(\text{RH})_\beta$ (96%/85%) (which is qualitatively similar to $f(\text{RH})_{neph}$ (85%/40%); Figure 4) is plotted against \mathring{a} . The data indicate that $f(\text{RH})_\beta$ (96%/85%) tends to increase with increasing \mathring{a} although the correlation is weak ($R=0.15$). This qualitative trend can be explained by the fact that at large \mathring{a} , there is a preponderance of small particles with low scattering efficiency. The effect of increasing RH is to allow these particles to grow to sizes at which they are more efficient scatterers. Sheridan et al. (2001) found, based on analysis of *in situ* data collected at SGP in 1999, that aerosols containing higher fractions of larger particles show larger hygroscopic growth factors. This is consistent with the trend for $f(\text{RH})_\beta$ vs \mathring{a} found here.

It is likely that $f(\text{RH})$ is closely tied to aerosol composition. For example, the water vapor uptake by inorganic salts is typically higher than for dicarboxylic organic acids. Also mixtures of inorganic and organic material

may exhibit suppressed deliquescence relative humidity (Raymond and Pandis, 2002). Since for non-IOP days aerosol composition data are unavailable, we use the single scattering albedo ω_o as a composition proxy to explore the effect of composition on $f(\text{RH})$. In Figure 11 $f(\text{RH})_\beta$ (96%/85%) is plotted as a function of ω_o for 8 out of a total of 17 cases that were available (only a limited number of absorption measurements, required for the determination of ω_o , was available due to instrument downtime). The range of ω_o is 0.922 to 0.980. The data show a weak positive correlation ($R=0.43$), but due to the sparseness of the data a clear trend cannot be deduced. We refer again to the study by Sheridan et al. (2001) who showed that aerosols containing higher fractions of more strongly absorbing particles exhibit lower hygroscopic growth factors. Delene and Ogren (2002) studied the behavior of ω_o as a function of the aerosol light scattering coefficient for data collected over a three and a half year period at the SGP site. They found that ω_o increased with increasing aerosol light scattering coefficient, i.e., that in cleaner conditions the aerosol that remains suspended is more absorbing. This implies, perhaps, that more absorbing aerosol particles are less hygroscopic, and perhaps less efficient CCN. Future studies will be required to clarify this hypothesis.

5 Discussion

5.1 Assessment of the method

The consistency between the measurements of $f(\text{RH})'_\beta$ and $f(\text{RH})'_{neph}$ described above should be considered in light of the following issues:

(a) a lidar measures 180° backscatter whereas a nephelometer measures total scattering. FM addressed this issue and showed with model calculations for marine type aerosol that for $\text{RH} < \sim 95\%$, $f(\text{RH})'_\beta \simeq f(\text{RH})'_{neph}$. However, the agreement may vary for different aerosol size distribution and composition;

(b) the two instruments measure over different RH ranges. We note that the general relationship between $f(\text{RH})'_\beta$ and $f(\text{RH})'_{neph}$ is closely related to the selected RH ranges for each instrument. Nephelometer $f(\text{RH})$ is commonly computed over a RH range from 40% to 85% and this has been adopted here. In the case of lidar we investigate three RH ranges to compute $f(\text{RH})'_\beta$ (85%, 96% and 98%) and find good correlation with $f(\text{RH})'_{neph}$ for both upper limits 96% and 98%;

(c) the lidar measures at 355 nm whereas the nephelometer measures at 450 nm. From model calculations we find that the effect of the wavelength

difference on backscatter and total scattering is closely tied to the aerosol size distribution and composition. Based on numerous calculations we can draw the following broad generalizations: (i) the more absorbing the particles, the larger are the differences between backscatter and total scattering (and hence in $f(\text{RH})_\beta$ and $f(\text{RH})_{neph}$) associated with the wavelength difference; (ii) the difference between backscatter and total scattering due to the wavelength difference seems to be less significant for smaller particles. These biases should be considered on a case-by-case basis.

(d) $f(\text{RH})_\beta$ is based on lidar profiling of the mixed layer, whereas $f(\text{RH})_{neph}$ is determined from in-situ ground based measurements in the surface layer. The surface layer is in general affected by surface processes on shorter time scales than the mixed layer. Apparently this did not significantly affect the current analysis except for the IOP day May 13 when the arrival of a frontal passage may have resulted in different aerosol properties within the surface layer and in the mixed layer. The fact that time averaged quantities were used rather than instantaneous measurements may have alleviated this problem;

(e) cloud base height has been determined here based on thermodynamic arguments rather than from lidar backscatter, as the range resolution is too coarse for this purpose. To obtain high accuracy in the cloud base determina-

tion using thermodynamic arguments it is important that the micrometeorological parameters be measured in the mixed layer, as was done here. Ideally, however, a lidar with high spatial resolution (order of meters) should be used as an additional measure of cloud base (see FM). Comparison between lidar- and thermodynamically-derived cloud base will provide a stronger criterion for well-mixed conditions and provide greater confidence in $f(\text{RH})_\beta$ at RH close to saturation.

6 Summary

A lidar technique that employs thermodynamic assumptions for well-mixed, cloud-capped boundary layers has been used to compute profiles of the hygroscopic growth factor $f(\text{RH})$ for ambient, unperturbed atmospheric conditions. The lidar-derived $f(\text{RH})$ over the range 85% RH to 96% RH correlate well with the growth factors from a collocated ground-based humidified nephelometer (40% RH to 85% RH). To our knowledge, This is the first observational evidence of the consistency between these two methods of deriving $f(\text{RH})$. The slopes of the growth curves reflect the fact that the growth over the range 85% RH to 96% RH is much stronger than over the range 40%

to 85%. The measurements were corroborated by a comparison of measured $f(\text{RH})$ with those computed based on *in situ* measurement of size distribution and composition for three cases during the May 2003 IOP.

We have investigated the possible relationship between aerosol size distribution and $f(\text{RH})_\beta$ using the Ångström exponent as a proxy for size distribution. The data suggest that $f(\text{RH})_\beta$ (96%/85%) increases with increasing \mathring{a} . A plausible explanation is that at high \mathring{a} , the dominance of smaller particles that are inefficient scatterers yields low backscatter, and their growth due to uptake of water vapor allows them to scatter more efficiently. At low \mathring{a} , the growth of the larger particles, that are already efficient scatterers, has less effect on $f(\text{RH})_\beta$. Preliminary investigation of the effect of aerosol composition (represented by the single-scattering albedo) shows a weak positive trend between $f(\text{RH})_\beta$ (96%/85%) and ω_o , but results are not conclusive. Due to the rather small number of data points analyzed, we cannot draw any conclusions regarding the suitability of ω_o as a proxy for aerosol composition. Further analyses are required to determine whether there is a clear relationship between $f(\text{RH})_\beta$ and ω_o .

The current study extends the prior demonstrations of this technique by Wulfmeyer and Feingold (2000) and FM and provides further confidence that

lidar can be a useful tool for measurement of aerosol growth, particularly at $RH > 85\%$. It is suggested that measurements of this kind will benefit greatly from higher lidar range resolution (on the order of meters) which will increase the accuracy of retrievals at RH approaching saturation.

Acknowledgments

The data used for this study were obtained from the Atmospheric Radiation Measurement (ARM) Program sponsored by the U. S. Department of Energy, Environmental Sciences Division. The authors thank the awarding agency as well as ARM staff for maintaining the instrumentation and the ARM database. This research was supported by the NOAA Postdoctoral Program in Climate and Global Change, administered by the University Corporation for Atmospheric Research.

References

- Boucher, O. and T. L. Anderson, 1995: General circulation model assessment of the sensitivity of direct climate forcing by anthropogenic sulfate aerosols to aerosol size and chemistry. *J. Geophys. Res.*, **100**, 26117-26134.
- Brechtel, F. J. and S. M. Kreidenweis, 2000: Predicting particle critical supersaturation from hygroscopic growth measurements in the humidified TDMA. Part II: Laboratory and ambient studies. *J. Atmos. Sci.*, **57**, 1872-1887.
- Charlson, R. J., S. E. Schwartz, J. M. Hales, R. D. Cess, J. A. Oakley Jr., J. E. Hansen, and D. J. Hofmann, 1992: Climate forcing by anthropogenic aerosols, *Science*, **255**, 423-430.
- Covert, D. S. and J. Heintzenberg, 1993: Size distribution and chemical properties of aerosol at Ny Alesund, Svalbard. *Atmos. Environ.*, **27A**, 2989-2997.
- Delene, D. J. and J. A. Ogren, 2002: Variability of aerosol optical properties at four North American surface monitoring sites, *J. Atmos. Sci.*, **59**,

1135-1150.

Dutton, J. A., 1976: *Dynamics of atmospheric motion*. Dover, New York, pp. 617.

Feingold, G. and B. Morley, 2003: Aerosol hygroscopic properties as measured by lidar and comparison with in situ measurements. *J. Geophys. Res.*, **108**, doi:10.1029/2002JD002842.

Ferrare, R. A., S. H. Melfi, D. N. Whiteman, K. D. Evans, M. Poellot, and Y. J. Kaufman, 1998: Raman lidar measurements of aerosol extinction and backscattering 2. Derivation of aerosol real refractive index, single-scattering albedo, and humidification factor using Raman lidar and aircraft size distribution measurements. *J. Geophys. Res.*, **103**, 19673-19689.

Goldsmith, J. E. M., S. E. Bisson, H. B. Blair, and D. D. Turner, 1998: Turn-key Raman lidar for profiling atmospheric water vapor, clouds, and aerosols. *Appl. Opt.*, **37**, 4979-4990.

Iribarne, J. V. and W. L. Godson, 1973: *Atmospheric Thermodynamics*. Reidel, Dordrecht, pp. 222.

Kasten, F., 1969: Visibility forecast in the phase of pre-condensation. *Tellus*,

21, 631-635.

Kotchenruther, R. A. and P. V. Hobbs, 1998: Humidification factors of aerosols from biomass burning in Brazil. *J. Geophys. Res.*, **103**, 32081-32089.

Kotchenruther, R. A., P. V. Hobbs, and D. A. Hegg, 1999: Humidification factors for atmospheric aerosols off the mid-Atlantic coast of the United States. *J. Geophys. Res.*, **104**, 2239-2251.

Malm, W. C., D. E. Day, S. M. Kreidenweis, J. L. Collett, and T. Lee, 2003: Humidity-dependent optical properties of fine particles during the Big Bend Regional Aerosol and Visibility Observational Study. *J. Geophys. Res.*, **108**, 4279, doi:10.1029/2002JD002998.

McInnes, L., M. Bergin, J. Ogren, and S. Schwartz, 1998: Apportionment of light scattering and hygroscopic growth to aerosol composition. *Geophys. Res. Lett.*, **25**, 513-516.

McMurry, P. H. and M. R. Stolzenburg, 1989: On the sensitivity of particle size to relative humidity for Los Angeles aerosols. *Atmos. Environ.*, **23**, 497-507.

Orsini, D. A., Y. Ma, A. Sullivan, B. Sierau, K. Baumann, and R. J. Weber,

- 2003: Refinements to the particle-into-liquid sampler (PILS) for ground and airborne measurements of water soluble aerosol composition. *Atmos. Environ.*, **37**, 1243-1259.
- Raymond, T. M. and S. N. Pandis, 2002: Cloud activation of single-component organic aerosol particles, *J. Geophys. Res.*, **107**, 4787, doi:10.1029/2002JD002159.
- Sheridan, P. J., D. J. Delene, and J. A. Ogren, 2001: Four years of continuous surface aerosol measurements from the Department of Energy's Atmospheric Radiation Measurement Program Southern Great Plains Cloud and Radiation Testbed site. *J. Geophys. Res.*, **106**, 20735-20747.
- Twomey, S., 1974: Pollution and the planetary albedo, *Atmos. Environ.*, **8**, 1251-1256.
- Vogelmann, A. M., P. J. Flatau, M. Szczodrak, K. M. Markowicz, and P. J. Minnett, 2003: Observations of large aerosol infrared forcing at the surface. *Geophys. Res. Lett.*, **30**, 1655, doi:10.1029/2002GL016829.
- Wulfmeyer, V. and G. Feingold, 2000: On the relationship between relative humidity and particle backscattering coefficient in the marine boundary layer determined with differential absorption lidar. *J. Geophys. Res.*,

105, 4729-4741.

Figure captions

Figure 1. Schematic illustrating the measurement range of nephelometer and lidar and the enhancement in scattering that aerosol undergoes for each respective range in RH.

Figure 2. Model parameter fit of $f(\text{RH})_\beta (= \beta(\text{RH})/\beta(85\%))$ to experimental data for RH ranging from 85% to 98%. The 17 cases that were available for analysis are shown. Routine measurement period data are shown as black lines and the IOP data are color coded (red: May 8; green: May 13; blue: May 17)

Figure 3. Comparison of the normalized $f(\text{RH})_\beta (90\%/85\%)/\Delta\text{RH}_\beta$ (where $\Delta\text{RH}_\beta = 5\%$) with $f(\text{RH})_{neph} (85\%/40\%)/\Delta\text{RH}_{neph}$ (where $\Delta\text{RH}_{neph} = 45\%$). Circles denote data obtained during the routine measurement period and square symbols represent data obtained during the IOP (red: May 8; green: May 13; blue: May 17). Error bars denote one standard deviation between the measured $f(\text{RH})$ and the $f(\text{RH})$ determined from the fit parameters.

Figure 4. Comparison of the normalized $f(\text{RH})_\beta (96\%/85\%)/\Delta\text{RH}_\beta$ (where $\Delta\text{RH}_\beta = 11\%$) with $f(\text{RH})_{neph} (85\%/40\%)/\Delta\text{RH}_{neph}$. Symbols and error

bars as in Figure 3. Additional symbols represent data computed with aerosol model. Diamonds represent results obtained for mean inorganic fraction. Upward (downward) pointing triangles were obtained for maximum (minimum) inorganic fraction during time period of interest.

Figure 5. Comparison of the normalized $f(\text{RH})_\beta (98\%/85\%)/\Delta\text{RH}_\beta$ (where $\Delta\text{RH}_\beta = 13\%$) with $f(\text{RH})_{\text{neph}} (85\%/40\%)/\Delta\text{RH}_{\text{neph}}$. Symbols and error bars as in Figure 3.

Figure 6. Mean aerosol size distributions measured on May 8 (red), 13 (green) and 17 (blue) during time periods that correspond to the lidar and nephelometer measurement periods (May 8: 15:10–15:50 UT, May 13: 16:20–16:50 UT; May 17: 18:10–18:30 UT).

Figure 7. Left column: Aerosol composition in terms of total mass (solid line), inorganic fraction (dashed line) and the difference between the two (dashed-dotted line); Right column: inorganic fraction; Top row: May 8, middle row: May 13 and bottom row: May 17

Figure 8. Normalized measured lidar and nephelometer backscatter and total scattering coefficients (circles) and normalized computed backscatter and total scattering coefficients from aerosol model (stars). The nor-

malized backscatter coefficients β_{norm} are shown in the left column and the normalized total scattering coefficients σ_{norm} are shown in the right column.

Figure 9. Time series of (a) total scattering coefficient σ_{sp} at 450 nm and (b) absorption coefficient σ_{ap} at 565 nm for May 13.

Figure 10. $f(\text{RH})_\beta$ (96%/85%) as a function of Ångström exponent \mathring{a} as determined from nephelometer at 700 nm and 450 nm. The error bars for \mathring{a} represent one standard deviation from the mean in \mathring{a} over the respective measurement period. Error bars for $f(\text{RH})_\beta$ (96%/85%) denote one standard deviation between the measured $f(\text{RH})_\beta$ and the $f(\text{RH})_\beta$ determined from the fit parameters. Symbols are as in Figure 3.

Figure 11. $f(\text{RH})_\beta$ (96%/85%) as a function of single scattering albedo ω_o as determined from the nephelometer at 450 nm and the light absorption photometer. The error bars for ω_o represent one standard deviation from the mean in ω_o over the respective measurement period. Error bars for $f(\text{RH})_\beta$ (96%/85%) denote one standard deviation between the measured $f(\text{RH})_\beta$ and the $f(\text{RH})_\beta$ determined from the fit parameters. Symbols are as in Figure 3.

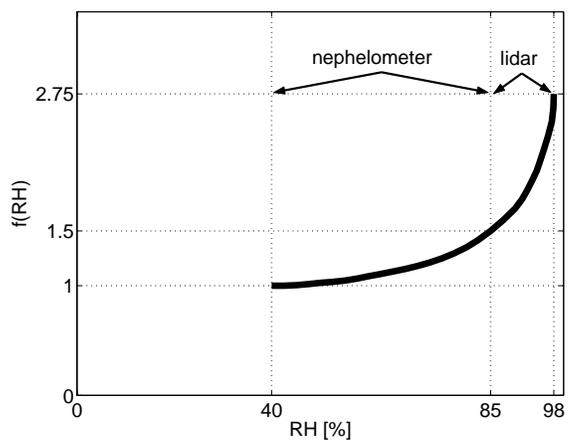


Figure 1:

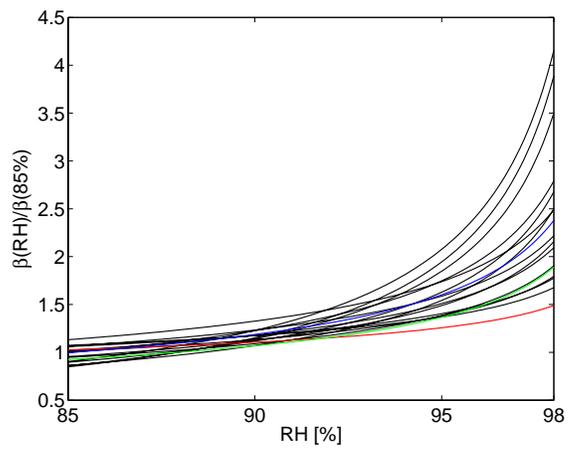


Figure 2:

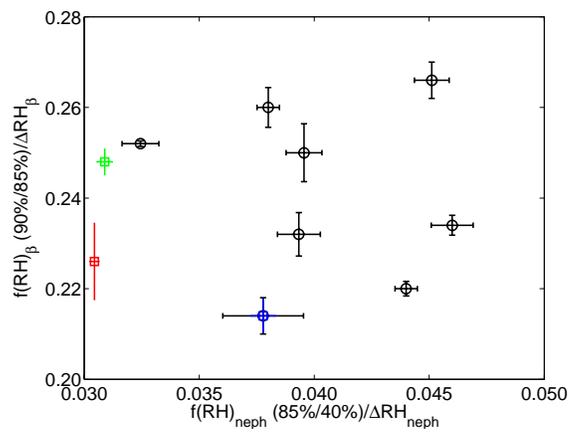


Figure 3:

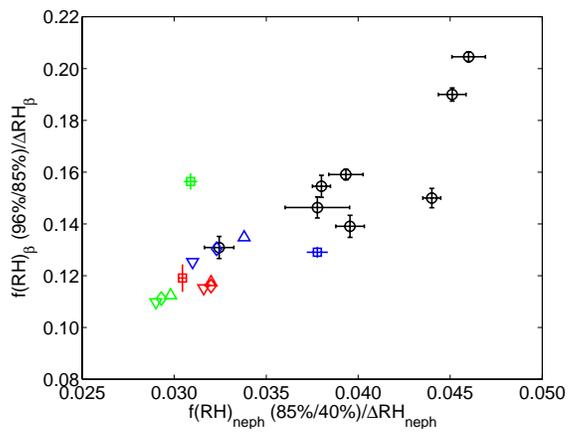


Figure 4:

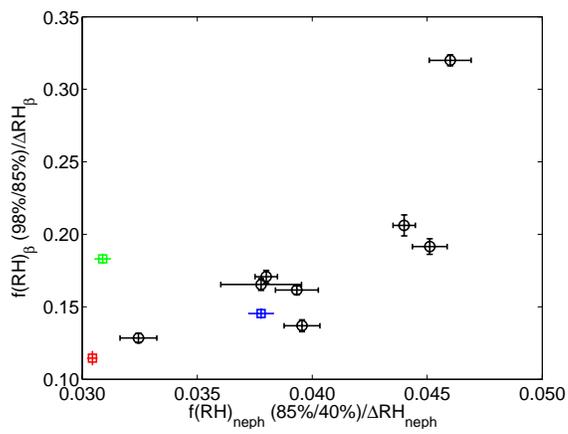


Figure 5:

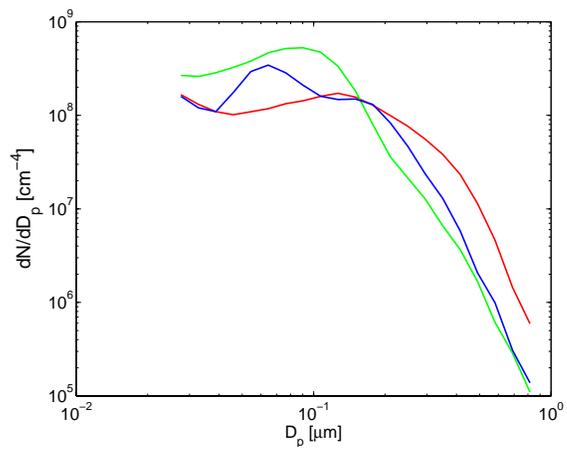


Figure 6:

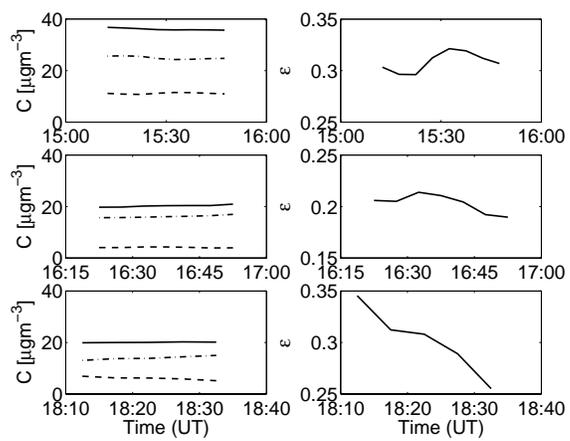


Figure 7:

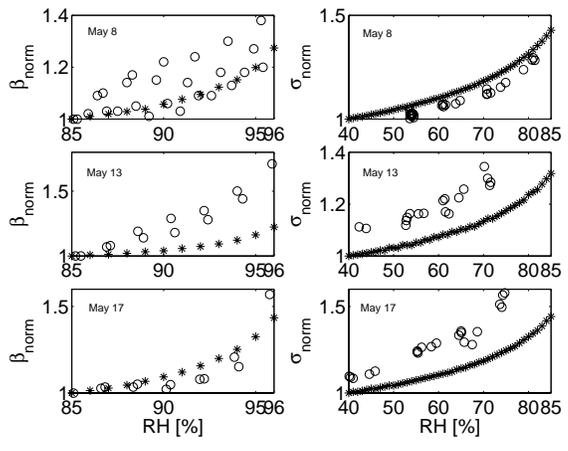


Figure 8:

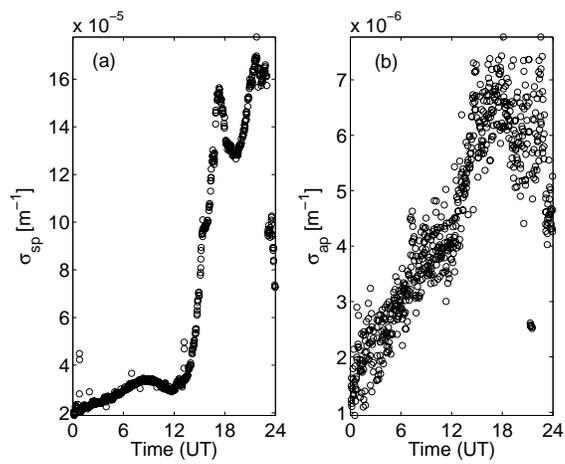


Figure 9:

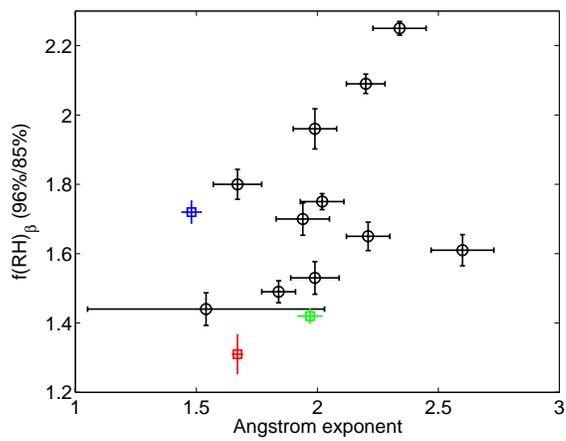


Figure 10:

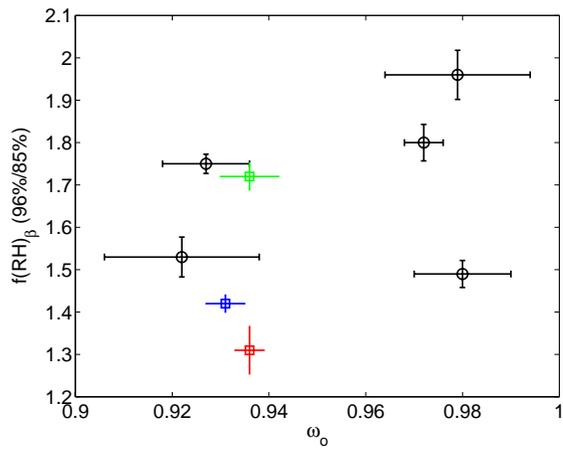


Figure 11: